

General existence and determination of conjugate fields in dynamically ordered magnetic systems

M. Quintana^{*} and A. Berger

CIC nanoGUNE BRTA, E-20018 Donostia-San Sebastian, Spain



(Received 13 July 2021; accepted 4 October 2021; published 21 October 2021)

We investigate experimentally as well as theoretically the dynamic magnetic phase diagram and its associated order parameter Q upon the application of a non-antisymmetric magnetic field sequence composed of a fundamental harmonic component H_0 , a constant bias field H_b , and a second-harmonic component H_2 . The broken time antisymmetry introduced by the second-harmonic field component H_2 leads to an effective bias effect that is superimposed onto the influence of the static bias H_b . Despite this interference, we can demonstrate the existence of a generalized conjugate field H^* for the dynamic order parameter Q , to which both the static bias field and the second-harmonic Fourier amplitude of the field sequence contribute. Hereby, we observed that especially the conventional paramagnetic dynamic phase is very susceptible to the impact of the second-harmonic field component H_2 , whereas this additional field component leads to only very minor phase-space modifications in the ferromagnetic and anomalous paramagnetic regions. In contrast to prior studies, we also observe that the critical point of the phase transition is shifted upon introducing a second-harmonic field component H_2 , illustrating that the overall dynamic behavior of such magnetic systems is being driven by the total effective amplitude of the field sequence.

DOI: [10.1103/PhysRevE.104.044125](https://doi.org/10.1103/PhysRevE.104.044125)

I. INTRODUCTION

Collective behaviors in systems with many degrees of freedom can lead to out-of-equilibrium pattern formations [1]. Such dynamically ordered states can be found in chemistry [2], biology [3], or physics [4–6]. Illustrative examples include brain activity [7], the formation of sand dunes [8,9], or information traffic flow [10]. One specific type of dynamic ordering known to happen in ferromagnetic spin systems was demonstrated to lead to a dynamic phase transition (DPT) [11], which has attracted a very significant amount of attention in recent years and has become a widely investigated phenomenon in the context of nonequilibrium physics [12–15]. The understanding of the DPT has provided very relevant insights about dynamically ordered systems and opened the door of using powerful scientific methods that had been developed originally for the study of thermodynamic phase transitions in equilibrium.

DPTs are known to be observable in ferromagnetic materials below the Curie temperature T_c [11]. Upon applying a sufficiently slow sinusoidal magnetic field $H(t)$ of period P and amplitude H_0 to such materials, the time response of the system's magnetization $M(t)$ will follow the magnetic field oscillations, as shown schematically by the red line in Fig. 1(a). Hereby, one typically observes a slight delay of $M(t)$ with respect to the field $H(t)$ due to the coercivity of the ferromagnet. However, if P becomes comparable to the system's relaxation time constant τ , there is a point at which the magnetization is not able to follow the magnetic field oscillations and does not reverse during the magnetic field cycle, but instead will exhibit only small oscillations around

one of two equivalent nonzero magnetization values, as shown by the red lines in Fig. 1(b). The green-dashed lines in Figs. 1(a) and 1(b) identify the period-averaged magnetization Q , defined as

$$Q = \frac{1}{P} \int_t^{t+P} M(t') dt'. \quad (1)$$

Thus, one observes here a fundamental change in the dynamic behavior of the magnetization trajectory as P is varied. In the slower dynamic regime, i.e., Fig. 1(a), the magnetization oscillates around a net zero magnetization value, resulting in $Q = 0$. This is known as the dynamic paramagnetic (PM) phase. In contrast, in the faster dynamics regime, displayed in Fig. 1(b), the magnetization oscillates around a $Q \neq 0$ average value, which is known as the dynamic ferromagnetic (FM) phase.

Hereby, Q represents the order parameter associated with the dynamic state, whose transition from the PM to the FM phase happens at a unique critical period P_c by means of a second-order phase transition [16]. This behavior is similar to that of the thermodynamic equilibrium case, in which M undergoes a temperature T dependent second-order phase transition at its Curie temperature T_c . Both the existence of the dynamic phase transition overall and scaling relations close to the critical point were verified by means of Monte Carlo simulations [16–18] and mean-field approximation (MFA) calculations [19,20]. These studies also confirmed the existence of critical exponents, which were furthermore found to be of the same universality class as the thermodynamic equilibrium case.

Upon adding an external time-independent bias field H_b to the sinusoidal magnetic field sequence, it was shown that H_b takes on the role of the conjugate field H^* of the dynamic

*m.quintana@nanogune.eu

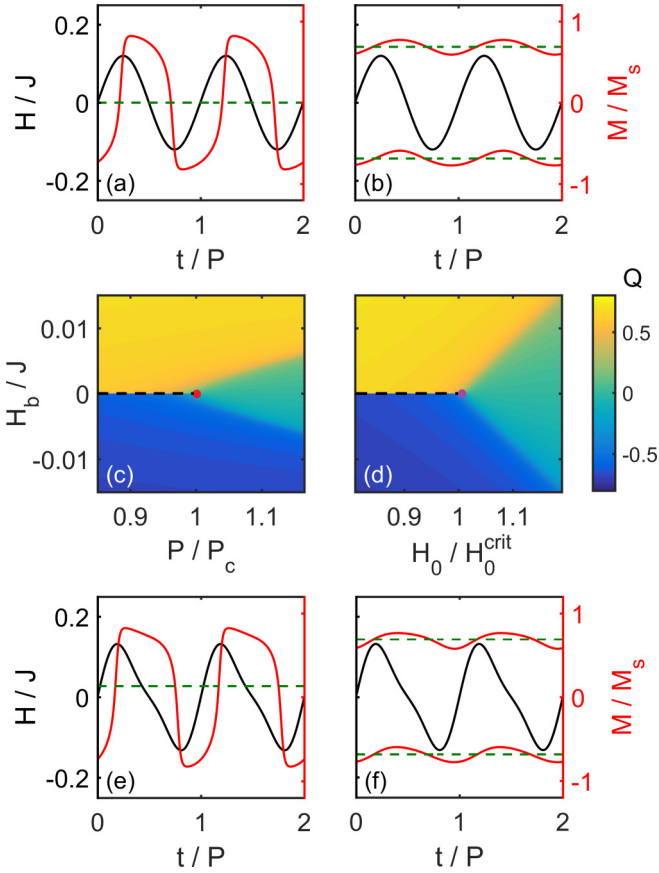


FIG. 1. (a), (b) Schematic examples of H (black) and the corresponding M (red) time sequences for two different P in the dynamic PM and FM regimes, respectively. The green-dashed lines represent the period-averaged magnetization Q . (c), (d) Color-coded maps of Q as a function of P/P_c (H_0/H_0^{crit}) and H_b in the vicinity of the DPT. The red (magenta) dot and the black-dashed line represent the second- and first-order phase transitions, respectively. The color bar, shown on the right-hand side, is valid for both (c) and (d). (e), (f) Schematic examples of H (black) and the corresponding M (red) time sequences in the dynamic PM and FM regimes with an additional H component of period $P/2$ being applied. The green-dashed lines represent the period-averaged magnetization Q .

order parameter Q [21], in the same way, in which an external magnetic field H is the conjugate field of magnetization M in the equilibrium phase diagram. This relevant discovery allowed for a far broader exploration of the DPT phenomenon, given that it enabled the characterization of a two-dimensional phase-space behavior for $Q(P, H^*)$. The identity of H_b being the conjugate field of Q was later verified in Ref. [20] when an analytical equation of state of the DPT was derived in the MFA model for the specific case of a sinusoidal driving field. In this context, experimental studies have played a most relevant role in the investigation of the existence of H^* and its impact on the dynamic state [22–25].

In Fig. 1(c) we show an illustrative example of this specific two-dimensional phase-space behavior of $Q(P, H^* = H_b)$ as a color-coded map and in the neighborhood of the critical point of the phase transition. In this map, one can distinguish a critical point at $P = P_c$, identified by means of a red

dot, dividing the FM and the PM phases. In the FM phase, two well-defined regions can be distinguished, which are the yellow and blue regions of the map. Here, upon increasing or decreasing H_b , Q undergoes a discontinuous first-order nonequilibrium phase transition at $H_b = 0$, labeled here as a black-dashed line. For $P > P_c$, in the PM phase, the change of Q as a function of H_b happens in a continuous fashion, and the changes in the blue-to-green and green-to-yellow regions are not abrupt, even if they can be rather steep due to the so-called metamagnetic anomalies of the paramagnetic dynamic state [23,26]. These metamagnetic anomalies divide a conventional PM region with $Q \sim 0$ for small enough values of $|H_b|$ (i.e., the predominantly green region in the map) from the anomalous PM region with large values of $|Q|$.

In absence of magnetostatic interactions, the dynamic magnetization behavior associated with the DPT is overall reflective of a spin-reversal mechanism that is triggered by an applied-field assisted nucleation process of inverted spin clusters, followed by the corresponding domain-wall propagation [16,17,27–29]. One direct consequence of this mechanism is that P_c is strongly dependent on the field amplitude H_0 used for the observation of the DPT, which follows a predominant $P_c \sim \exp(\text{const.}/H_0)$ behavior [16,17]. Correspondingly, one can explore the relevant phase space near the DPT including its critical behavior in two different ways. The behavior of Q close to the critical point can be explored in the (P, H_b) phase space leaving H_0 constant [i.e., Fig. 1(c)] or in the (H_0, H_b) space leaving P constant. Figure 1(d) shows a representative phase space of $Q(H_0, H_b)$. Here, one finds a qualitatively identical map to the $Q(P, H_b)$ case in Fig. 1(c), with the main difference being the shape of the conventional PM region for small values of $|H_b|$. The critical field amplitude H_0^{crit} , represented as a magenta dot in Fig. 1(d), is the field amplitude at which $P = P_c$. Experimental phase-space investigations in the (H_0, H_b) approach allow for a broader exploration of the complete phase space, as we have previously demonstrated experimentally [24,25], so that we will follow this approach here as well.

In most works that study the DPT, the oscillating components of the time-dependent $H(t)$ sequences that are applied to the magnetic system exhibit the so-called half-wave antisymmetry (HWA), meaning that $H(t) = -H(t + P/2)$. This antisymmetry condition in $H(t)$ holds for both sinusoidal magnetic fields, mainly used in MFA works [19,20,30] and experiments [22–25], and for squarelike magnetic fields, commonly used in Monte Carlo simulations [14–18,31,32]. In the dynamic PM phase, the HWA of the magnetic field also implies that $M(t) = -M(t + P/2)$ [33], which naturally leads to $Q = 0$ for the order parameter. However, if one now considers an oscillatory field sequence that breaks the HWA, the magnetization trajectory will not be antisymmetric either in between the two half periods, which can lead to a nonzero value of Q even in the absence of H_b . As an illustration of this phenomenon, we show in Fig. 1(e) the magnetization response for a $H(t)$ sequence composed by two in-phase Fourier components of period P and $P/2$ with $H_b = 0$, such that the HWA of $H(t)$ is broken. We observe that the $M(t)$ antisymmetry is lost as well, leading to an average magnetization $Q \neq 0$, even if the magnetization goes through a full reversal cycle. It is therefore clear that H^* cannot be

simply identical to H_b here because the absence of H_b does not lead to a vanishing order parameter in this dynamic PM state.

Indeed, the role of higher-order frequencies was first investigated in Ref. [34], where the effects of different Fourier components were independently studied. Interestingly, it was found that any even Fourier field component can contribute to H^* , while odd components do not contribute here given that these components do not break the HWA. Furthermore, each even component was observed to follow independently the same scaling behavior at P_c . However, the impact of even components in conjunction with a static bias field onto the dynamic phase and the occurrence of the DPT has not been investigated yet, and thus the issue of H^* existence and definition for any general $H(t)$ sequence has not been addressed.

We emphasize that our qualitative discussion above is limited to the dynamic PM phase for simplicity. In the dynamic FM phase, illustrated in Fig. 1(f), a difference in between the two existent $M(t)$ trajectories (and the subsequent values of Q) for $H_b = 0$ is still existent, but it is much smaller than in the PM phase and visually hard to detect in contrast to the obvious modifications visible in Fig. 1(e). However, from our discussion it is evident that there is a need to develop a generally applicable definition of the conjugate field H^* in the context of an arbitrary $H(t)$ sequence. If it exists, such a generalized conjugate field should fulfill specific requirements. Particularly, H^* has to guarantee that dynamically stable states fulfill time-reversal symmetry, i.e.,

$$Q(H^*) = -Q(-H^*), \quad (2)$$

for all values of P (and H_0), analogous to the usual thermodynamic response of ferromagnets in equilibrium phase space, where $M(H) = -M(-H)$ for all temperature and field values (see for example Ref. [35]). For the case of simple sinusoidal magnetic driving field [i.e., Figs. 1(c) and 1(d)], it is clear that H_b fulfills this condition and thus justifies the identity $H_b = H^*$.

The general identification of H^* is crucially relevant in the context of the DPT, because proper knowledge of what H^* is exactly, is needed to actually explore the dynamic phase space and conduct meaningful studies. This condition does not only apply to two-dimensional (H_0, H^*) phase-space explorations, but also to the more traditional one-dimensional phase-space explorations along the H_0 - or P -axes, because for them to be insightful, they have to be conducted under the condition that $H^* = 0$, which requires an actual quantitative knowledge of H^* . To date, no general formulation and analysis of H^* for general $H(t)$ sequences has been developed. Therefore, we explore in the present work the proper definition and determination of the conjugate field H^* for general $H(t)$ sequences, both analytically and experimentally, by utilizing asymmetric time-dependent magnetic field sequences in conjunction with static bias fields throughout the complete phase space near the DPT. Hereby, we will explore the general existence of H^* and we will establish a generally applicable procedure to obtain H^* . We will also explore the specific impact that even-order Fourier components of magnetic field sequences have onto the critical point itself.

In the second section of this work, we present the theoretical and experimental methods employed in our study. First, we present the MFA model used to simulate the dynamic mag-

netization trajectories throughout the dynamic phase space. Then, we present the most relevant experimental aspects regarding our sample design and fabrication, and we discuss some key aspects of the transverse magneto-optical Kerr effect (T-MOKE) setup that we used to measure individual $M(t)$ trajectories and determine associated Q values. In the third section, we discuss our main findings resulting from our MFA model calculations and in the fourth section, we compare them to the experimentally obtained results. Finally, in the fifth and last section we draw general conclusions, put the results into perspective of prior studies, and give an outlook beyond our present work.

II. METHODS

We have computed the dynamic behavior of magnetization trajectories for an Ising spin system. The most commonly used model in the context of DPTs is the kinetic Ising model with spin $s = 1/2$. In such system, each spin s_i interacts with the nearest neighbors via an exchange-coupling constant J and with the external magnetic field $H(t)$ through a Zeeman energy term, leading to the Hamiltonian

$$\mathcal{H} = -J \sum_{\langle i,j \rangle} s_i s_j - H(t) \sum_i s_i, \quad (3)$$

where the brackets stand for the sum over nearest neighbors only.

In this work, we focus on a time-dependent magnetic field signal with three different Fourier components. The first two components are the most commonly utilized terms, namely the bias field H_b and the fundamental of period P and amplitude H_0 . The third component is an in-phase second-harmonic contribution of period $P/2$ and amplitude H_2 . Thus, the complete field sequence is described as

$$H(t) = H_b + H_0 \cos\left(\frac{2\pi t}{P}\right) + H_2 \cos\left(\frac{4\pi t}{P}\right). \quad (4)$$

Assuming that the system evolves under standard Glauber stochastic dynamics [36], the MFA equation of motion of $M(t)$ can be expressed as [11]

$$\tau \frac{dM(t)}{dt} = -M(t) + \tanh\left(\frac{1}{T} \left[M(t) + \frac{H(t)}{J} \right]\right), \quad (5)$$

with T being the temperature normalized to T_c . We evaluate Eq. (5) to obtain a steady-state periodic solution of $M(t)$. Details regarding the self-consistent evaluation of (5) can be found in the Appendix. All simulations in this work are done at the reduced temperature $T = 0.8$, for which only second-order dynamic phase transitions occur, even within MFA [19]. This avoids possible complications due to the appearance of a first-order phase transitions upon changing P , which are an associated artifact of the mean-field approach at lower temperatures [37,38].

In the kinetic Ising model described by Eq. (3), magneto-static interactions are not considered because demagnetizing fields suppress the bistable behavior and the correspondingly sharp onset of the dynamic order parameter at the dynamic phase transition, similar to the behavior of equilibrium phase transitions, where magnetostatic effects lead to a

self-demagnetization of bulklike ferromagnets in the thermodynamic ferromagnetic phase. This approach of neglecting magnetostatic effects has been used in all theoretical treatments of the DPT so far, given that it reduces the complexity of dynamic ferromagnetic systems. In order to mimic the dynamic behavior of such an Ising model without demagnetizing fields experimentally, thin film samples with in-plane magnetization geometry have been specifically designed and employed in the past, because in this configuration, demagnetizing fields are strongly suppressed and clear observations of the DPT are possible [19,24,25]. Furthermore, these works employed thin films with uniaxial magnetic anisotropy with the easy axis (EA) of magnetization in the plane of the film, such that only two stable states are existent at zero field, and all core aspects of the Ising model can be reproduced.

Following prior work, we utilize here a 20-nm-thick Co (10 $\bar{1}0$) thin-film structure prepared by a DC-magnetron sputter deposition in an ultrahigh vacuum (UHV) deposition system (ATC series, AJA International, Inc.) with a base pressure better than 10^{-7} mTorr. In order to promote the epitaxial growth of such a Co film, a single-crystal substrate and a specific layer sequence is required [39,40], which is shown schematically as an inset in Fig. 2(a). As substrates, we use hydrofluoric-acid-etched Si wafers with (110) surface orientation. On top of each Si (110) surface, a 40-nm-thick Ag (110) film and a 10-nm Cr (211) film are deposited to produce a suitable template layer, which promotes the desired epitaxial growth of the 20-nm Co (10 $\bar{1}0$) film. On top of the Co layer, a 10-nm-thick SiO $_2$ film is deposited by rf sputtering in the same UHV chamber, which prevents the oxidation of our samples. X-ray diffraction (XRD) measurements were carried out in order to verify the intended epitaxial structure of our samples. Figure 2(a) shows θ -2 θ scan data with the diffraction peaks corresponding to the crystallographic planes of Co (10 $\bar{1}0$), Si (220), Ag (220), Cr (211), and Co (20 $\bar{2}0$). The SiO $_2$ film grows amorphous and does not show any peak. The observation of the second-order Co (20 $\bar{2}0$) peak and the absence of diffraction peaks corresponding to other crystallographic planes verify the intended epitaxial structure of our samples and their excellent crystallographic quality.

Vibrating sample magnetometry measurements were carried out in order to test the in-plane uniaxial magnetic anisotropy that it expected for the above-mentioned crystallographic structure of our samples. Specifically, we measured the magnetization component parallel to the direction of the field, which is applied in the plane of the film for different azimuthal orientations of the sample. Figure 2(b) shows the remanent magnetization M_r normalized to saturation M_s , as a function of the in-plane angle φ in between the EA and the direction of the field. The values are obtained at zero field after previously applying a field that is strong enough to saturate the magnetization along any given direction. The sample exhibits the expected sinusoidal angular dependence with a 180° periodicity. Furthermore, $M_r/M_s = 1$ for $\varphi = 0^\circ, 180^\circ$ and its value reduces in textbook fashion as the sample is rotated towards the hard axis, i.e., $\varphi = 90^\circ, 270^\circ$. The solid black line shows the expected ideal behavior [41], which is in excellent agreement with the experimental data. Thus, by means of our structural and static magnetic characterization measurements, we confirmed that our samples exhibit the

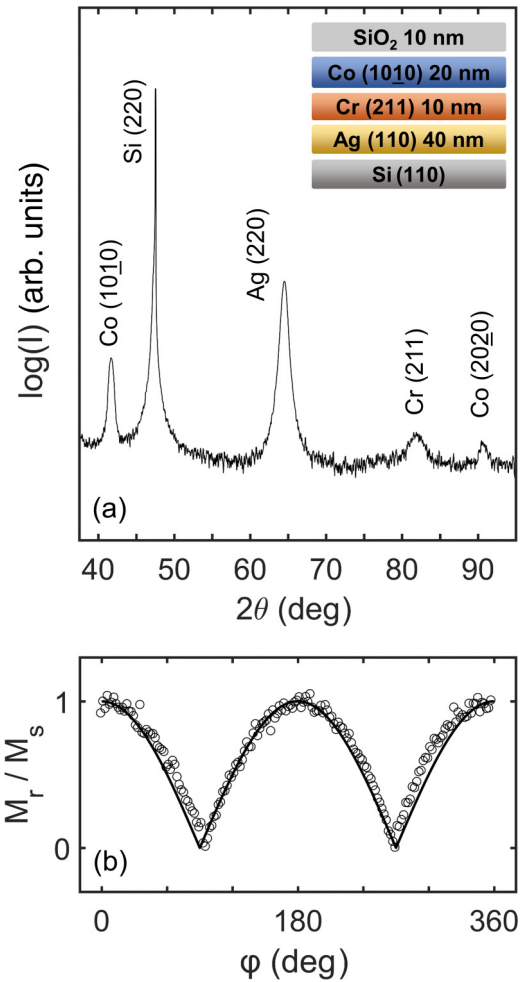


FIG. 2. (a) θ -2 θ XRD scan showing the diffraction intensity peaks of an epitaxial Co (10 $\bar{1}0$) film. The epitaxial growth sequence is shown as a schematic inset in the figure. (b) Normalized remanent magnetization M_r/M_s vs the field orientation angle φ after saturation, showing the expected uniaxial anisotropy. The solid black line represents the perfect textbook behavior of uniaxial samples.

intended in-plane uniaxial magnetic anisotropy required for the study of dynamic magnetic behavior in the presence of non-antisymmetric magnetic field sequences and their impact onto the conjugate dynamic field H^* of order parameter Q .

In order to precisely measure the magnetization vs time behavior of our samples, we employ a transverse magneto-optical Kerr effect setup, which is particularly suitable for our thin-film samples due to its excellent surface sensitivity [24,25,42,43]. A schematic of the tool is shown in Fig. 3(a). Here, we employ an ultralow-noise laser with $\lambda = 635$ nm and an output power of 5 mW. Our specific setup measures the magneto-optically induced ellipticity changes in the reflected light intensity, which are proportional to the transversal magnetization component only [42,43]. The setup utilizes an angle of incidence of 60° with respect to the surface normal. The first polarizer P_1 is oriented in such a way that the incident beam is linearly polarized at 45° with respect to the plane of incidence, and thus is a linear combination of s - and p -polarized light components of equal intensity. In the reflected beam arm of our setup, the quarter-wave plate

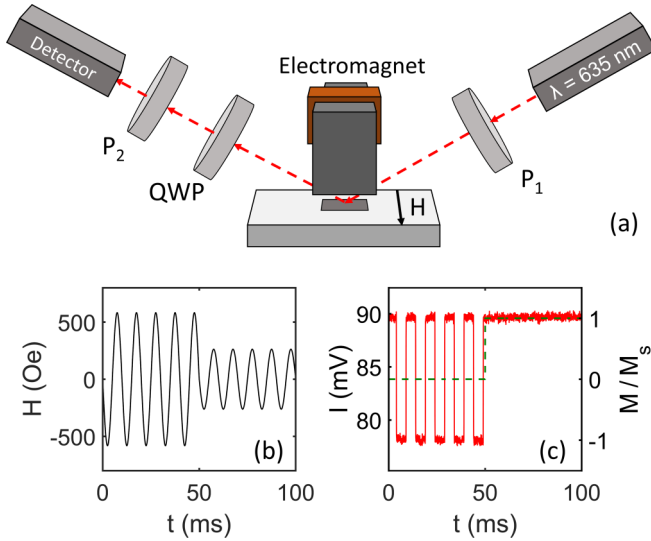


FIG. 3. (a) Experimental T-MOKE setup scheme consisting of a coherent light source with $\lambda = 635$ nm, an initial polarizer P_1 , a quarter-wave plate QWP, a second polarizer P_2 , and a photodetector. The U-shaped electromagnet is located above the sample and produces a magnetic field H parallel to the sample surface and normal to the optical plane of incidence at the point of the laser light spot. (b) Exemplary experimental H vs t sequence representing two different field amplitudes. (c) Synchronously measured M vs t data using the T-MOKE system. The dashed line illustrates the period-averaged magnetization (Q).

(QWP) is aligned to remove the purely optical ellipticity that occurs after light reflection from the sample and the second polarizer P_2 is aligned in a nearly crossed position to the polarization state emerging from the QWP. This particular optical configuration leads to very large relative light-intensity changes upon magnetization reversal and achieves an excellent signal-to-noise ratio, so that real-time $M(t)$ sequences can be measured and analyzed. Further details of our specific setup and its underlying detection scheme can be found in Refs. [42,43].

In Figs. 3(b) and 3(c), we show exemplary experimental $H(t)$ and $M(t)$ curves, respectively. Figure 3(b) shows ten periods of $H(t)$ representing two different field amplitudes. Figure 3(c) shows the simultaneously measured light-intensity signal that is measured with the sample's EA being aligned along the direction of the field. The first five field periods, measured while applying a magnetic field amplitude of 582.2 ± 0.1 Oe, show an almost perfect square pattern with only two stable magnetic states, as expected in our uniaxial sample for fields that are sufficiently large to trigger a magnetization reversal. Figure 3(c) also demonstrates the excellent signal-to-noise ratio as well as the very large relative light-intensity change upon magnetization reversal, which is larger than 10% of the average intensity value. The first five periods of the signal are used here as reference data to calibrate the complete signal sequence to the saturated magnetization states $M_s = \pm 1$. In this regime, the magnetization undergoes full hysteresis loops, leading to a $Q = 0$ value, represented by the green-dashed line, which is the expected behavior in the dynamic PM phase. In contrast, the subsequent five field os-

cillations with a field amplitude of 262.2 ± 0.1 Oe result in a magnetization vs time sequence that remains at all times very close to one of the two saturated states, and whose value is determined by the last half period of the preceding stronger field amplitude. In this case, $Q \approx 1$, as one can see from the green-dashed lines, which is the expected behavior in the dynamic FM phase far away from the critical point. Thus, Fig. 3 demonstrates that we can access both the dynamic FM and PM phases by properly tuning H_0 and at the same time achieve an extremely high magnetization sensitivity in our T-MOKE tool.

In order to properly characterize the phase space of the DPT experimentally, we measure 300 periods for fixed field conditions and subsequently evaluate the time-averaged order parameter (Q) from the magnetization vs time sequences. Then, we decrease or increase H_b stepwise while keeping the rest of the parameters constant, so that we can effectively access the dynamically stable state in the entire phase space, including regions close to the first-order phase transition line in the FM phase, where Q vs H_b hysteresis phenomena have to be considered [19]. Reference signals are measured before and after each measurement sequence, so that our intensity signal traces are always properly normalized and possible light-intensity drifts can be compensated. These drift compensations were extremely small for all measurements in this study due to the excellent sensitivity and stability of our T-MOKE system [25].

III. SIMULATION RESULTS

In this section, we will theoretically analyze the effects of a nonzero H_2 component onto the overall phase-space behavior of Q close to the critical point, as well as address the question of the general existence of a conjugate H^* field in the presence of both H_b and H_2 . If it exists, a general formulation of H^* needs to be consistent with time-reversal symmetry, as explained in Sec. I. Such a generalized H^* should be in principle compatible with an expansion around $H^* = H_b$, at least for sufficiently small H_2 values, because $H^* = H_b$ is valid in the absence of dynamic field components that break the HWA of $H(t)$.

In order to characterize the viability of such an expansion and following the methodology explained in Sec. II, we study first the impact of a H_2 term onto the PM phase for fixed P/τ and H_0/J values, because in this region of the phase space, deviations from the $H^* = H_b$ case seem to be very substantial, according to Figs. 1(e) and 1(f). In Fig. 4(a), we present examples of dynamic behavior by showing the Q vs H_b dependence in the PM phase for several values of H_2/J with $P/\tau = 50$ and $H_0/J = 0.1$. For the $H_2 = 0$ case [i.e., the blue line in Fig. 4(a)], Q describes the expected behavior of the dynamic PM phase. Here, Q increases monotonously with H_b in an antisymmetric fashion, as expected according to Eq. (2), and we verify that $Q(H_b = 0) = 0$. We can clearly distinguish here the conventional PM region, with an almost linear increase of Q for small enough values of $|H_b|$, and an anomalous PM region for large $|H_b| > 0.02J$ values, in which Q is nearly saturated. Both the conventional and anomalous PM regions are separated by the metamagnetic onset regions [23], which are characterized by steep increases of Q with H_b .

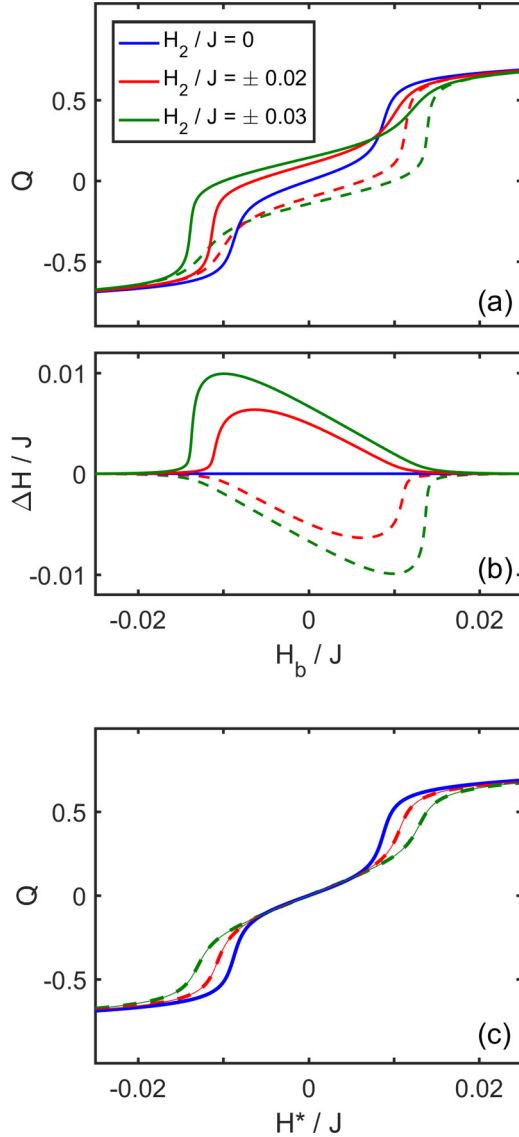


FIG. 4. (a) MFA simulation results of Q vs H_b for several H_2 amplitudes in the PM phase with $P/\tau = 50$ and $H_0/J = 0.11$. (b) Corresponding deviations ΔH vs H_b required to recover the expected time-reversal symmetry for the same values of H_2 shown in (a). (c) Q vs H^* computed by using Eqs. (6) and (7) for the datasets shown in (a) and (b).

For nonzero values of H_2 , the anomalous PM regions differ only minimally from the $H_2 = 0$ case in the way Q approaches its near-saturation value as a function of H_b . However, the behavior in the conventional PM phase differs substantially. Here, with increasing H_2 , Q shows an offset “quasiplateau” of increasing magnitude. For opposite values of H_2 , Q displays the same behavior but with negative quasiplateau values for Q , as demonstrated by the dashed lines in Fig. 4(a). The deviations from the $H_2 = 0$ case come from the fact that the driving force of the dynamics is asymmetric and thus, the resulting magnetization dynamics is asymmetric too, leading to an effective bias effect. The nonzero H_2 component also affects the shape of the metamagnetic regions of the map. Here, we observe a shift of the metamagnetic onset regions as well as a broadening in the change of Q with H_b in only

one of the two metamagnetic transition regions. Overall, we find that these results are fully consistent with the data shown in Fig. 1(e), in which Q was found to be nonzero for $H_b = 0$.

The fact that the antisymmetry of the Q vs H_b curve is not preserved in the PM region implies that $H^* \neq H_b$ upon the application of additional harmonic components in the driving magnetic field sequence. In order to verify the possible existence of a generalized expression of the conjugate field $H^*(H_b, H_2)$, we first define the deviation $\Delta H(H_b, H_2)$ of H^* from the pure bias field value H_b , such that

$$H^* = H_b + \Delta H(H_b, H_2). \quad (6)$$

This deviation ΔH is the change in field required to recover Eq. (2), which can be obtained as the net bias shift in-between two opposite values of Q , namely

$$\Delta H = \frac{1}{2}[H_b(Q) + H_b(-Q)], \quad (7)$$

where Q is implicitly dependent on H_b and H_2 . In Fig. 4(b), ΔH is shown as a function of H_b for the cases displayed in Fig. 4(a). We see that ΔH describes an asymmetric nearly triangular shape as a function of H_b whose magnitude has the same sign as H_2 , and furthermore vanishes for $H_2 = 0$. Also, we see that ΔH approaches zero in the regions corresponding to the anomalous PM region, which implies that the nearly saturated Q state is not substantially affected by H_2 , at least in this segment of the phase space.

Figure 4(c) shows the same set of Q data now as a function of H^* , calculated by means of Eqs. (6) and (7). Here, we see that the antisymmetry is completely restored for all selected H_2 amplitudes. The values of Q with opposite H_2 collapse onto the same curve if plotted against the H^* axis. These results indeed verify that a generalized conjugate field H^* can be computed by means of Eqs. (6) and (7), at least in the PM phase, so that time-reversal symmetry is restored [44].

In order to provide a complete description of the effects of H_2 close to the critical point of the DPT, we present in Figs. 5(a)–5(e) Q as a function of H_0/J and H_b/J for several values of H_2/J . For the $H_2 = 0$ case in Fig. 5(c), we find the previously described conventional phase-space behavior, as already described in Sec. I in conjunction with Fig. 1(d). Below the critical field amplitude $H_0^{\text{crit}}/J = 0.101$, i.e., in the dynamic FM phase, there are two well-defined regions with opposite values of $Q \neq 0$ upon reversal of H_b . In the PM phase for $H_0 > H_0^{\text{crit}}$, we observe that $Q = 0$ for $H_b = 0$ and changes continuously as a function of H_b . In summary, the time-reversal symmetry is strictly preserved in the complete phase space with H_b being identical to the conjugate field H^* .

For nonzero values of H_2 , the FM phase remains almost unchanged in agreement with the behavior observed in Fig. 1(f), with the exceptions being the exact location of the critical point and the precise placement of the phase line that separates the dynamically stable states, which we will discuss later. In the FM phase, Q shows very similar values in all cases upon increasing $|H_2|$, as seen from the yellow and blue areas in the maps. In the anomalous PM regions of the maps, the values of Q are also not substantially affected by a nonzero H_2 component. However, in the conventional PM phase Q shows a clear offset behavior that increases in size with H_2 , which can be identified by the gradual color change in between Figs. 5(a)–5(e) in the conventional PM regions of the phase

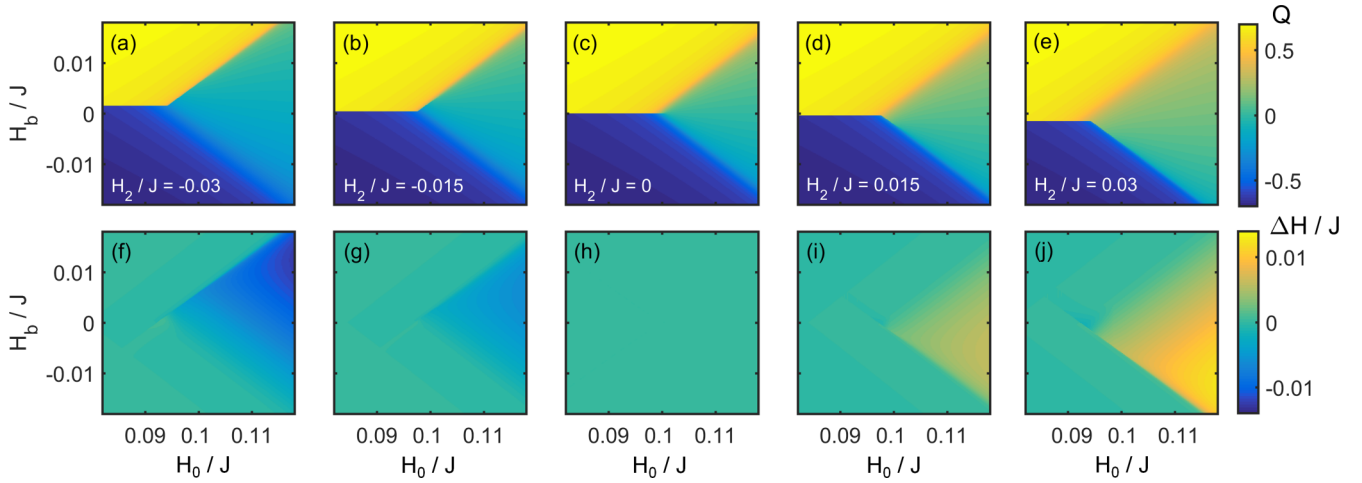


FIG. 5. (a)–(e) Color-coded maps of Q in the analyzed phase space around the DPT as a function of H_0 and H_b for several values of H_2 . (f)–(j) Color-coded maps of ΔH for the corresponding phase spaces in (a)–(e) as a function of H_0 and H_b . The color bars, shown on the right-hand side of (e) and (j), are valid for the entirety of each respective row.

space. This change of Q in the conventional PM phase agrees with the results in Fig. 4(a), in which this offset behavior was displayed for one specific H_0/J value. As already mentioned, there is a shift of the critical point for increasing $|H_2|$. For the $|H_2|/J = 0.03$ case, for instance, H_0^{crit} is about 4% smaller than in the $H_2/J = 0$ case. This shift is due to the fact that the maximum field due to the superposition of the H_0 and H_2 components is larger, and thus only a smaller H_0 value is required to drive the system into the PM phase. These findings demonstrate that the addition of secondary harmonic field components to the usual magnetic field sequence affects both H^* and the critical point of the overall phase space, contrary to what was previously reported [34]. Further details regarding the critical point evolution upon changing H_2 will be discussed in Sec. IV in conjunction with the corresponding experimental results.

Given that H_b does not properly represent the conjugate field in the phase space now, the phase line dividing the stable states of Q in Figs. 5(a)–5(e) is ill defined in the H_b domain [22]. So, for simplicity we utilize the shift of the critical point in the (H_0, H_b) domain, which can be easily identified, to decide where the transition of all dynamically stable states occurs along the H_b axis for all $H_0 < H_0^{\text{crit}}$ values. Correspondingly, this shift of the critical point away from the $H_b = 0$ point for nonvanishing H_2 values leads to a shifting of the line dividing the positive and negative states of Q in the entire FM phase. This shift is, however, very modest in size and can only be spotted upon very close inspection of Fig. 5. It is also noticeable that, as in Fig. 4(a), there is an asymmetry in the metamagnetic onset upon introducing nonvanishing H_2 values, which persists for all values of H_0 .

Figures 5(f)–5(j) show the corresponding deviations ΔH , according to Eq. (7), required to transform H_b into H^* for each $H_0/J, H_b/J$ point in the phase space. As expected, the deviations are zero within the numerical precision of our computations in the complete phase space for $H_2 = 0$, as seen in Fig. 5(h). As H_2 increases, the deviations become increasingly large in the conventional PM phase only and exhibit the same sign as H_2 itself. These results are a generalization of the

corresponding results in Fig. 4(b). The values of ΔH in both the anomalous PM region and the FM phase are at least two orders of magnitude smaller (but still nonzero) in comparison with the central portion of the PM region. These results agree with the fact that the phase space in the FM region remains basically unaltered, with the only exception being the phase line dividing the stable states.

We therefore conclude that the addition of secondary Fourier components to the magnetic field signal plays a substantial role only in the conventional PM phase, as well as for the exact location of the critical point. We observe that the secondary harmonic field acts as an effective additional bias field that works in sync or against H_b . We verify that a H^* field exhibiting the properties of the conjugate field can be constructed even in the presence of H_2 . We have also shown how to construct such a H^* field and have analyzed the characteristic of the needed correction to H_b in the entirety of the relevant phase space.

IV. EXPERIMENT RESULTS

To verify the relevance of our theoretical observations, we will now analyze the experimental phase-space behavior of $\langle Q \rangle$ in our Co (10 $\bar{1}$ 0) sample and compare these results with the simulations of Sec. III. The measurements were carried out in our T-MOKE setup at room temperature with the fundamental period of the field oscillations being $P = 10$ ms. In Figs. 6(a)–6(e), we show the experimental phase-space behavior of $\langle Q \rangle$ as a function of both H_0 and H_b for several values of H_2 . In all the cases, the order parameter shows a qualitative identical behavior to the simulations in Figs. 5(a)–5(e). For the $H_2 = 0$ Oe case in Fig. 6(c), the phase-space behavior of $\langle Q \rangle$ is characterized by a critical point at $H_0^{\text{crit}} = 314.9$ Oe dividing both the FM and the PM phases. In the FM phase, for $H_0 < H_0^{\text{crit}}$, we observe two well-defined opposite regions separated by the $H_b = 0$ phase line. In the dynamic PM phase, $\langle Q \rangle = 0$ within the experimental precision for $H_b = 0$ and reaches near saturation for sufficiently large values of H_b in the anomalous PM phase. Also, in our experiments here, the

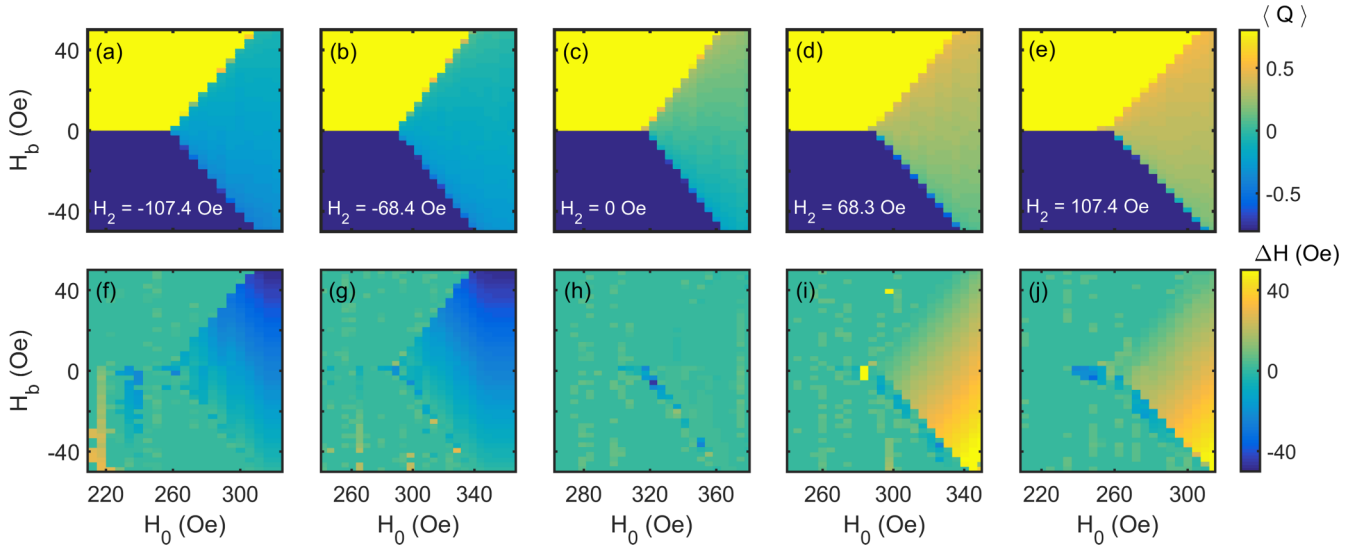


FIG. 6. (a)–(e) Color-coded maps of $\langle Q \rangle$ in the analyzed phase space around the DPT as a function of H_0 and H_b for several values of H_2 . (f)–(j) Color-coded maps of experimental ΔH for the corresponding phase spaces in (a)–(e) as a function of H_0 and H_b . The color bars, shown on the right-hand side of (e) and (j), are valid for the entirety of each respective row.

metamagnetic anomalies happen in a rather narrow range of H_b field values that are of the order of our experimental resolution along the H_b axis in our large area measurements, as seen by the seemingly abrupt yellow-to-green and green-to-blue transition regions.

For different H_2 values in Figs. 6(a)–6(e), the phase transition and the phase-space behavior of $\langle Q \rangle$ is not fundamentally changed. In all the cases, there is a FM and a PM phase clearly divided by a critical field amplitude H_0^{crit} . However, one can most evidently observe here that the values of $\langle Q \rangle$ in the conventional PM regime increase monotonously with H_2 , in good agreement with the simulations shown in Figs. 5(a)–5(e). Furthermore, the critical field amplitude decreases substantially with $|H_2|$, leading to $H_0^{\text{crit}} = 255.4$ Oe for $H_2 = \pm 104.7$ Oe, which is fundamentally consistent with the results in Sec. III, even if it represents a yet more substantial decrease than what occurs in our simulations. In the FM phase, any deviation from the $H_2 = 0$ case is smaller than the H_b resolution grid that we were able to employ experimentally. Correspondingly, possible shifts of the phase line dividing the stable states in the FM phase are below our H_b resolution. Nonetheless, it is clearly observed that all core characteristics of the phase-space behavior of $\langle Q \rangle$ are in very good qualitative agreement with the simulations in Sec. III. As in the simulations, we observe also here that the secondary field component affects mainly the conventional PM phase, as well as the critical field amplitude whose relative difference is found to be larger than in our simulations.

Figures 6(f)–6(j) show as color-coded maps the corresponding experimental $\Delta H(H_0, H_b)$ values, determined by using Eq. (7) in the entirety of the measured phase space and for the same H_2 amplitudes used for Figs. 6(a)–6(e). For the $H_2 = 0$ Oe case in Fig. 6(h), ΔH is effectively zero in the entire analyzed phase space, except for the region with very large metamagnetic fluctuations, which is simply a consequence of the experimental resolution limit along the H_b axis and thus leads to an enhanced noise level for the determined

ΔH values. As H_2 is varied, ΔH shows a qualitative identical phase-space behavior to the one found in the simulations, as can be seen in Figs. 6(f)–6(j). Also, here we observe that the higher-order induced bias ΔH is only relevant in the conventional PM phase. We identify an asymmetric shape as a function of H_b whose magnitude increases monotonously with H_2 , also in good agreement with the results in Figs. 5(f)–5(j). The ΔH values in the FM phase are smaller than the fluctuation level of our measurements, and thus are equal to zero within our experimental precision.

In Fig. 7(a), we show $\langle Q \rangle$ along a cut of the phase space in the PM state, in which H_0 is kept constant at $1.08 H_0^{\text{crit}}$ while H_b is varied for three different values of H_2 . Here, we clearly see that the change of $\langle Q \rangle$ due to the presence of H_2 is significant in the conventional PM region only, which is in excellent qualitative agreement with our MFA simulations shown in Fig. 4(a). We also observe that the H_b range of the conventional PM regime is similar in these cases, which is associated with the fact that we chose a fixed H_0/H_0^{crit} ratio. We observe a substantial impact of H_2 onto the general occurrence of the metamagnetic anomalies only in creating an asymmetry in the $\langle Q \rangle$ change that is associated with them, which is essentially the same behavior as seen in the calculations. In contrast to the calculations, however, we do not observe an asymmetric broadening of only one of the metamagnetic onset regions, which might be associated with the limited resolution in H_b that we can achieve experimentally.

To analyze the observed effective bias effect of H_2 in the conventional PM phase in a more quantitative manner, we computed as a function of H_2 the average value of $\langle Q \rangle$ at $H_b = 0$ for the same H_0/H_0^{crit} ratio, a quantity we call Q_0 and display in Fig. 7(b). For small H_2 amplitudes, Q_0 increases linearly but, as H_2 becomes increasingly large, the slope decreases, and the behavior becomes sublinear. This analysis is fully consistent with the results of our simulations shown in the inset of Fig. 7(b) that displays a very similar qualitative behavior.

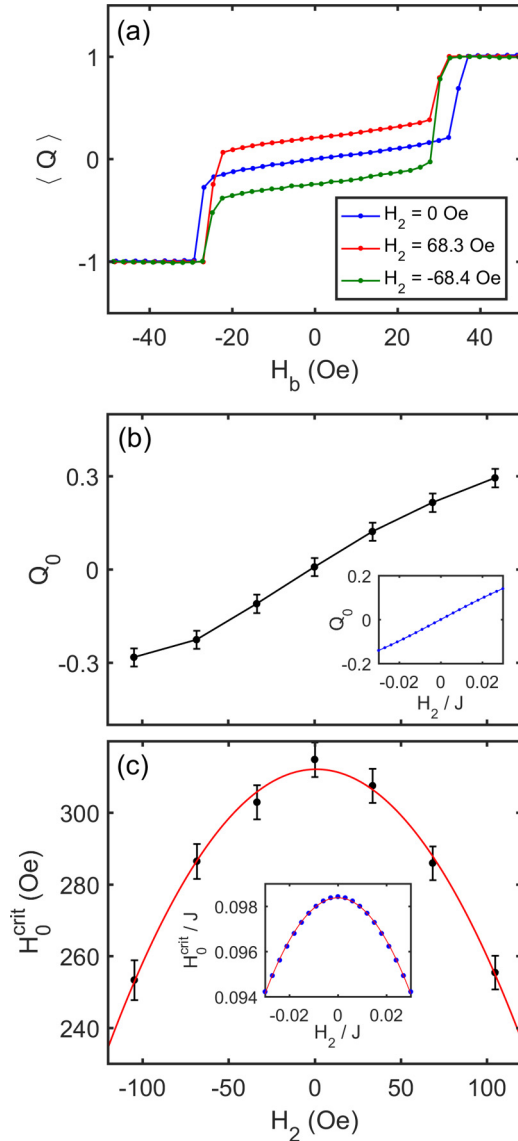


FIG. 7. (a) Experimental $\langle Q \rangle$ vs H_b for several H_2 and $H_0 = 1.08 H_0^{\text{crit}}$. (b) Experimental value of $\langle Q \rangle$ at $H_b = 0$ for $H_0 = 1.08 H_0^{\text{crit}}$ as a function of H_2 . The inset figure shows as a comparison the corresponding simulated results for the same H_0/H_0^{crit} ratio. (c) Experimental H_0^{crit} as a function of H_2 . The inset figure shows as a comparison the simulated H_0^{crit} as a function of H_2 . The red lines correspond in both cases to a least-square fit to a parabolic function centered at $H_2 = 0$.

Another aspect that we have analyzed in detail is the H_2 dependence of the critical point. Figure 7(c) shows the experimental H_0^{crit} values as a function of H_2 . The inset of the figure shows comparatively the simulated results for H_0^{crit}/J . In both cases we identify a quadratic decrease of the critical field amplitude as a function of H_2 . The red lines represent a least-squares fit to a parabolic function centered around $H_2 = 0$, providing in both cases a very large coefficient of determination $R^2 > 0.995$. This behavior is explained by the fact that as $|H_2|$ increases while keeping H_0 constant, the total field amplitude also increases. Correspondingly, the total amplitude of $H(t)$ can become larger than H_0^{crit} for the H_2 -free case,

and the system will transition into the dynamic PM phase, even if H_0 alone is smaller than the critical field amplitude. Thus, by increasing H_2 , while keeping H_0 constant, H_0^{crit} will decrease. We observed here that the H_0^{crit} vs H_2 dependence is quadratic, at least for a substantial range of H_2 . We are also mindful of the fact that there is a one-to-one correspondence in between H_0^{crit} and P_c determining the location of the critical point, as explained in Sec. I. Thus, one can deduce that for increasing H_2 , P_c should decrease in a similar fashion as H_0^{crit} , which is differing from what was previously reported in Ref. [34], where H_2 and higher even Fourier amplitudes of the field sequence were only associated with producing a bias effect. To our understanding, this difference seems to be related to the fact that the authors of Ref. [34] investigated very small values of the higher Fourier amplitudes only, i.e., $H_2 \ll H_0$, because their focus was on the scaling behavior of Q in a region of the phase space very close to the critical point. Correspondingly, the values of H_2 amplitudes used in this previous study were probably too small in comparison to the fundamental amplitude to detect any noticeable change in P_c .

However, we also recognize that the relative change of H_0^{crit} with H_2 differs substantially in between simulations and experiments. While the relative change of H_0^{crit} is on the order of 4% in the simulations with respect to the maximum H_2/J value used in our study, the experimental results indicate a relative change of 30%. At the same time, the slope of Q_0 with H_2 , shown in Fig. 7(b), also seems to differ in between simulations and experiments by about 30% in units of field normalized to H_0^{crit} . In relation to these quantitative differences, we emphasize that experiments and simulations are done in very different P/τ parameter ranges and thus both systems show very different relaxation timescales. Also, our simulations here correspond to a MFA model in which spin fluctuations are neglected. These details might contribute to the observed quantitative mismatch of the impact that H_2 has on the dynamic state of a ferromagnetic system, but whose qualitative behavior is nonetheless in very good agreement in between simulations and experiments.

To complete our in-depth analysis and provide an overall perspective of the presented results, it is worthwhile to consider the following general aspects of our observations regarding ΔH for both experiments and simulations. Figure 8(a) shows $\Delta H/H_0^{\text{crit}}$ as a function of the normalized bias field H_b/H_0^{crit} for several H_2 values and for a fixed $H_0 = 1.08 H_0^{\text{crit}}$. Here, we observe that the three curves show very prominent triangular shapes whose width is nearly identical in all three cases. The range of significant ΔH values fully coincides with the conventional PM regime. Figure 8(b) shows as a comparison the $\Delta H/H_0^{\text{crit}}$ vs H_b/H_0^{crit} for the same $H_0/H_0^{\text{crit}} = 1.08$ ratio. In this case, we also observe an asymmetric near-triangular shape in all the cases, with magnitudes being similar to those in Fig. 8(a). Here, the behavior close to the maximum is far smoother than for the experimental data given the substantially higher H_b resolution that can be achieved in the theoretical study. The vertical black-dashed lines stand for the local maxima of the metamagnetic susceptibility, which clearly confine the region of very large ΔH values. The relative width is different in between simulations and experiments, due to the fact that different effective P/τ

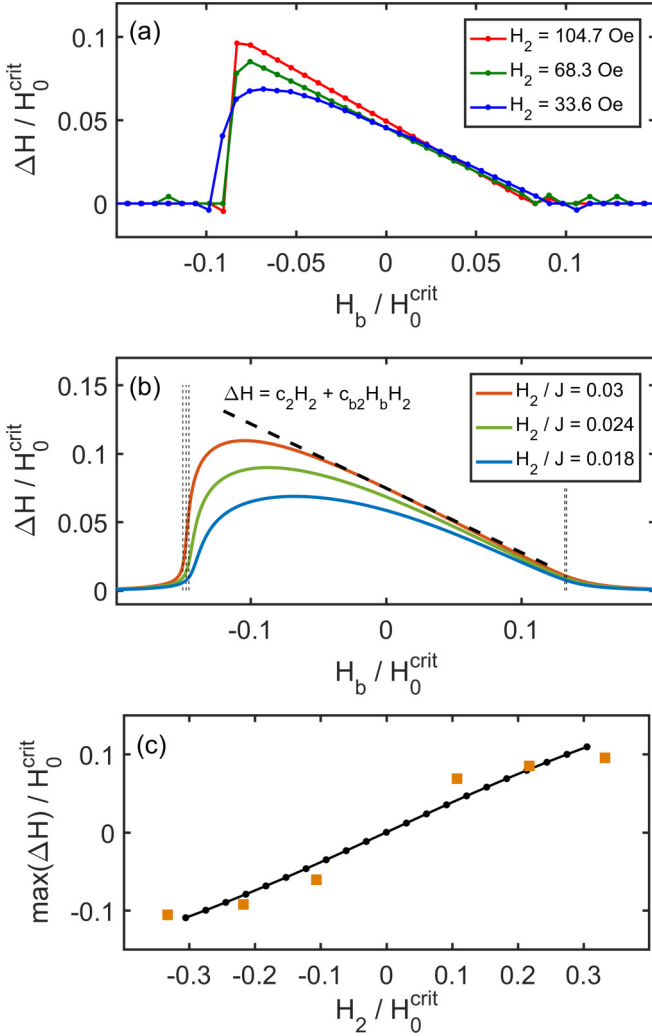


FIG. 8. (a) Experimental $\Delta H/H_0^{\text{crit}}$ data as a function of H_b/H_0^{crit} for several H_2 values and $H_0/H_0^{\text{crit}} = 1.08$. (b) Simulated $\Delta H/H_0^{\text{crit}}$ data as a function of H_b/H_0^{crit} for several H_2/J with the same H_0/H_0^{crit} ratio and $P/\tau = 50$. The thick black-dashed line represents the deviations $\Delta H = c_2 H_2 + c_{b2} H_b H_2$ for the $H_2/J = 0.03$ case, which are shown to be valid only for small values of $|H_b|$. (c) Normalized maximum amplitude of ΔH . Black points represent simulation results whereas the colored squares represent experimental data.

values are being used, which lead to different opening angles of the conventional PM region in the normalized dynamic phase space [12].

Figures 8(a) and 8(b) show that the width of the deviations ΔH in the renormalized space is identical in all the cases. Thus, the widening of ΔH with H_2 in the PM phase space that was observed in Fig. 4(b) is simply due to the H_0^{crit} vs H_2 dependence rather than a genuine widening of the conventional PM region itself. In other words, H_2 affects the critical point, but the shape of the conventional PM region remains basically unaltered in the properly renormalized H_0/H_0^{crit} scale.

Figure 8(c) shows the observed maximum of $\Delta H/H_0^{\text{crit}}$ as a function H_2/H_0^{crit} . The simulated points, shown as black dots, show an almost linear increase with H_2 , in agreement with the almost linear increase of Q_0 with H_2 observed in Fig. 7(b). The colored points represent the experimental

$\max(\Delta H)/H_0^{\text{crit}}$ values, and both experiments and simulations agree well in the magnitude of $\Delta H/H_0^{\text{crit}}$. For larger H_2/H_0^{crit} values, the experimental $\max(\Delta H)/H_0^{\text{crit}}$ seem to saturate relevantly, which is not observed in the simulation behavior. This difference might be associated with the fact that the experimental $\Delta H/H_0^{\text{crit}}$ vs H_b/H_0^{crit} curves appear somewhat truncated and thus, their actual measured maximum might be slightly reduced in comparison to the respective theoretical curves for large H_2 values.

Finally, it is worthwhile to make some general remarks regarding the nontrivial shape and nonlinear behavior of the deviations ΔH , and analyze their origin. In Ref. [34], it was observed that each even Fourier component produces the same scaling behavior independently that one would expect from a conjugate field, which led to the proper conclusion that each such component contributes to the conjugate field. This finding can be utilized to make the initial assumption that the generalized conjugate field could be estimated by a simple superposition of the even Fourier components, such that $H^* = H_b + c_2 H_2 + c_4 H_4 + \text{etc.}$. If this were correct, then the deviation ΔH would be $\Delta H = c_2 H_2 + c_4 H_4 + \text{etc.}$, which is equivalent to a simple linear shift of the $Q(H_b)$ curves. However, Fig. 4(a) already reveals that the modifications to the actual $Q(H_b)$ curves are far more substantial than that and we observe instead a far more severe nonsymmetric appearance, especially in the metamagnetic regions, which are affected in a very asymmetric manner. This behavior indicates that the contributions of the even components onto the conjugate field are not simply additive but contain very significant correlation effect.

In order to visualize this correlation in its simplest form, we have considered bilinear corrections, such that $H^* = H_b + c_2 H_2 + c_{b2} H_b H_2$, where the prefactor c_{b2} describes the strength of this correlation if both H_b and H_2 are present. As an example, we show in Fig. 8(b) how the deviation $\Delta H = c_2 H_2 + c_{b2} H_b H_2$ appears for the $H_2 = 0.03J$ case within this bilinear approximation. The bilinear correction fits our full solution for small enough values of $|H_b|$, while at the same time demonstrating that the correlated bilinear term is relevant for all H_b values, even the smallest ones. Thus, a mere superposition of the conjugate field contributions for each H_{2j} is inherently unsuitable due to the strong correlated effect that the different field components have on the dynamic behavior and the order parameter. Even if allowing for the bilinear inclusion of correlated effects, Fig. 8(b) shows that the correction is not applicable in the complete phase space along the H_b direction. Furthermore, we find that the set of coefficients (c_2, c_{b2}) are H_0 dependent and thus, they do not lead to meaningful or broadly applicable results in this direction of the phase space either, which is emblematic for the strong correlated effect of all the different field amplitudes onto the dynamic system, including H_0 . Correspondingly, we find a series expansion approach of H^* not very meaningful, if one attempts to cover a very significant part of the dynamic phase space, which was our intent here. For smaller subsections of the phase space, such an approach might be useful, though, even if in all likelihood a large number of expansion terms will have to be considered to accurately describe such a nonlinear magnetic system, whose precise dynamic state depends on the correlated net effect of all external field components.

In this regard, we emphasize that our approach is inherently valid in the complete parameter space and is not restricted to small values of H_b or H_2 . Both the simulations and experiments point at very specific symmetry conditions in $\Delta H(H_b, H_2)$, as well as the phase-space behavior of Q in the presence of a general $H(t)$ sequence. In the absence of H_2 , the inversion of $H_b \rightarrow -H_b$ in the magnetic field signal leads to exactly $Q \rightarrow -Q$. At the same time, in the absence of H_b , we observed that the inversion of $H_2 \rightarrow -H_2$ also leads to $Q \rightarrow -Q$, as one can see for example in Figs. 4(a) and 4(b). However, if both H_b and H_2 are nonzero, the $Q \rightarrow -Q$ state is accessed with $H_b \rightarrow -H_b$ and $H_2 \rightarrow -H_2$. This antisymmetric feature is necessarily preserved in the deviations so that $\Delta H(H_b, H_2) = -\Delta H(-H_b, -H_2)$, which is what we observe in the entirety of our investigation. Correspondingly, it is easy to show that $H^*(H_b, H_2) = -H^*(-H_b, -H_2)$, which in and by itself is not a trivial observation.

V. CONCLUSIONS

In this work, we studied the overall phase-space behavior of a dynamic magnetic system, for which a second-harmonic field contribution is superimposed to a conventional field sequence used in the context of the DPT, which normally contains only a fundamental sinusoidal and a constant bias field contribution. We observed that the fundamental characteristics of the phase-space behavior are preserved with the dynamic order parameter Q defining clearly identifiable FM and PM phases, separated by a critical point, and the characteristic occurrence of metamagnetic anomalies in the PM state. However, we also observe that such a second-harmonic field component plays a substantial role in modifying several relevant aspects of the phase-space behavior. Most fundamentally, the conjugate field of the order parameter needs to be redefined and the position of the critical point is relevantly shifted.

Firstly, we observed that the second-harmonic field contribution acts as an additional bias field whose effects are most visible in the conventional PM phase. Nonetheless, we have demonstrated that a proper conjugate field can be constructed as a function of the field amplitudes of the even Fourier components and time-reversal symmetry can be restored in the complete phase space if an adequately corrected conjugate field is considered. We obtained a generalized procedure to calculate this conjugate field considering an expansion around the conventional bias field. We also demonstrate the viability of this approach for experimental and simulated data for varying amplitudes of the second-harmonic field contribution.

Overall, the results of our work are in excellent agreement with those in Ref. [34], with the only difference being that no shift of the critical point as a function of the second-harmonic field amplitude H_2 was reported in this previous work. We believe that this difference is related to the very small higher-order field amplitudes that were utilized in Ref. [34] in conjunction with the quadratic dependence of the critical point shift with H_2 that we observed. Our results imply that the critical point of the phase transition is being determined by the total amplitude of the field oscillations, which is indeed composed by all Fourier components except for the bias field.

It should be noted that, in this work, we have focused our attention onto the influence of a secondary in-phase harmonic field component of period $P' = P/2$ only. However, it

is reasonable to expect that higher-order even Fourier components should contribute similarly to the overall dynamic system behavior in the phase space near the DPT, possibly with an order-dependent decreasing relevance given that the corresponding periods are increasingly further away from the periods close to the critical region. Higher-order odd Fourier components might also alter the dynamic behavior and the exact location of the critical point, but they should not play any role in the conjugate field given that these field components do not break the HWA of the field sequence, which is consistent with numerous Monte Carlo studies, that typically apply a rectangular field sequence to trigger the dynamic behavior.

Thus, we have addressed the issue of a generalized conjugate field in a comprehensive manner and observed that the conjugate field of the dynamic order parameter is not solely composed of the bias field in the most general scenario. Instead, this generalized conjugate field can be determined from sufficiently complete phase-space data. It should be interesting to verify whether the critical behavior close to the critical point conserves the values of its critical exponent with respect to the newly constructed conjugate field, an aspect that is beyond the scope of this work.

ACKNOWLEDGMENTS

Our work was supported by the Spanish Ministry of Science and Innovation under the Maria de Maeztu Units of Excellence Programme (Grant No. MDM-2016-0618) and Project No. RTI2018-094881-B-100 (MCIU/Feder), as well as by Predoctoral Fellowship No. PRE2019-088428.

APPENDIX

In order to obtain the steady-state periodic solutions of $M(t)$ following Eq. (5), we evaluate the corresponding finite difference equation,

$$\begin{aligned} M(k) &= F[M(k)] \\ &= \frac{1}{1 + \tau K/P} \left[\tanh \left(\frac{1}{T} \left[M(k) + \frac{H(k)}{J} \right] \right) \right. \\ &\quad \left. + \frac{\tau K}{P} M(k-1) \right], \end{aligned} \quad (\text{A1})$$

with $K = 300$ being the number of discrete time points k in a period for our simulations. In order to solve Eq. (A1), we consider an initial condition $M_{i=1}(k) = \pm 0.15 + 0.4 \sin(2\pi k/K)$ and self-consistently evaluate $M_i(k)$ as

$$M_i(k) = M_{i-1}(k) + s[F[M_{i-1}(k)] - M_{i-1}(k)], \quad (\text{A2})$$

where $s = 0.5$ represents the fraction of $F[M_{i-1}(k)]$ added to the next iteration in order to keep the iteration procedure stable. The cutoff for the convergence of $M(k)$ is set at

$$\max(F[M_i(k)] - M_i(k)) < 10^{-10}, \quad (\text{A3})$$

which is sufficient to provide reliable solutions in the entirety of the explored phase space. Afterwards, following Eq. (1), the order parameter is numerically obtained for each $M(k)$ as

$$Q = \frac{1}{K} \sum_{k=1}^K M(k). \quad (\text{A4})$$

- [1] M. C. Cross and P. C. Hohenberg, *Rev. Mod. Phys.* **65**, 851 (1993).
- [2] C. E. Woodward, M. Champion, and D. J. Isbister, *J. Chem. Phys.* **116**, 2983 (2002).
- [3] I. Shmulevich, S. A. Kauffman, and M. Aldana, *Proc. Natl. Acad. Sci. USA* **102**, 13439 (2005).
- [4] J. Kröll, J. Darmo, S. S. Dhillon, X. Marcadet, M. Calligaro, C. Sirtori, and K. Unterrainer, *Nature (London)* **449**, 698 (2007).
- [5] A. Shekhawat, S. Zapperi, and J. P. Sethna, *Phys. Rev. Lett.* **110**, 185505 (2013).
- [6] D. Bonamy, S. Santucci, and L. Ponsón, *Phys. Rev. Lett.* **101**, 045501 (2008).
- [7] V. K. Jirsa and H. Haken, *Phys. Rev. Lett.* **77**, 960 (1996).
- [8] J. L. Hansen, M. van Hecke, A. Haaning, C. Ellegaard, K. H. Andersen, T. Bohr, and T. Sams, *Nature (London)* **410**, 324 (2001).
- [9] G. W. Baxter, R. P. Behringer, T. Fagert, and G. A. Johnson, *Phys. Rev. Lett.* **62**, 2825 (1989).
- [10] M. Takayasu, H. Takayasu, and K. Fukuda, *Physica A* **277**, 248 (2000).
- [11] T. Tomé and M. J. de Oliveira, *Phys. Rev. A* **41**, 4251 (1990).
- [12] P. Riego, P. Vavassori, and A. Berger, *Physica B* **549**, 13 (2018).
- [13] J. D. Alzate-Cardona, H. Barco-Ríos, and E. Restrepo-Parra, *Phys. Lett. A* **382**, 792 (2018).
- [14] E. Vatansever and N. G. Fytas, *Phys. Rev. E* **97**, 062146 (2018).
- [15] E. Vatansever, *Phys. Lett. A* **381**, 1535 (2017).
- [16] S. W. Sides, P. A. Rikvold, and M. A. Novotny, *Phys. Rev. Lett.* **81**, 834 (1998).
- [17] S. W. Sides, P. A. Rikvold, and M. A. Novotny, *Phys. Rev. E* **59**, 2710 (1999).
- [18] G. Korniss, C. J. White, P. A. Rikvold, and M. A. Novotny, *Phys. Rev. E* **63**, 016120 (2000).
- [19] O. Idigoras, P. Vavassori, and A. Berger, *Physica B* **407**, 1377 (2012).
- [20] R. A. Gallardo, O. Idigoras, P. Landeros, and A. Berger, *Phys. Rev. E* **86**, 051101 (2012).
- [21] D. T. Robb, P. A. Rikvold, A. Berger, and M. A. Novotny, *Phys. Rev. E* **76**, 021124 (2007).
- [22] A. Berger, O. Idigoras, and P. Vavassori, *Phys. Rev. Lett.* **111**, 190602 (2013).
- [23] P. Riego, P. Vavassori, and A. Berger, *Phys. Rev. Lett.* **118**, 117202 (2017).
- [24] J. M. Marín Ramírez, E. Oblak, P. Riego, G. Campillo, J. Osorio, O. Arnache, and A. Berger, *Phys. Rev. E* **102**, 022804 (2020).
- [25] M. Quintana, E. Oblak, J. M. Marín Ramírez, and A. Berger, *Phys. Rev. B* **102**, 094436 (2020).
- [26] G. M. Buendía and P. A. Rikvold, *Phys. Rev. B* **96**, 134306 (2017).
- [27] P. A. Rikvold, H. Tomita, S. Miyashita, and S. W. Sides, *Phys. Rev. E* **49**, 5080 (1994).
- [28] A. Kirilyuk, J. Ferre, and D. Renard, *J. Magn. Magn. Mater.* **171**, 45 (1997).
- [29] G. Korniss, P. A. Rikvold, and M. A. Novotny, *Phys. Rev. E* **66**, 056127 (2002).
- [30] P. Riego and A. Berger, *Phys. Rev. E* **91**, 062141 (2015).
- [31] M. Acharyya, *Phys. Rev. E* **56**, 1234 (1997).
- [32] M. Acharyya, *Phys. Rev. E* **69**, 027105 (2004).
- [33] N. Fujiwara, T. Kobayashi, and H. Fujisaka, *Phys. Rev. E* **75**, 026202 (2007).
- [34] D. T. Robb and A. Ostrander, *Phys. Rev. E* **89**, 022114 (2014).
- [35] N. Goldenfeld, *Lectures on Phase Transitions and the Renormalization Group* (CRC Press, Boca Raton, FL, 1992).
- [36] R. J. Glauber, *J. Math. Phys.* **4**, 294 (1963).
- [37] G. Berkolaiko and M. Grinfeld, *Phys. Rev. E* **76**, 061110 (2007).
- [38] X. Shi and G. Wei, *Phys. Lett. A* **374**, 1885 (2010).
- [39] O. Idigoras, U. Palomares, A. K. Suszka, L. Fallarino, and A. Berger, *Appl. Phys. Lett.* **103**, 102410 (2013).
- [40] O. Idigoras, A. K. Suszka, P. Vavassori, B. Obry, B. Hillebrands, P. Landeros, and A. Berger, *J. Appl. Phys.* **115**, 083912 (2014).
- [41] E. C. Stoner and E. P. Wohlfarth, *Philos. Trans. R. Soc. London* **240**, 599 (1948).
- [42] E. Oblak, P. Riego, L. Fallarino, A. Martínez-de-Guerenu, F. Arizti, and A. Berger, *J. Phys. D: Appl. Phys.* **50**, 23LT01 (2017).
- [43] E. Oblak, P. Riego, A. Garcia-Manso, A. Martínez-de-Guerenu, F. Arizti, I. Artetxe, and A. Berger, *J. Phys. D: Appl. Phys.* **53**, 205001 (2020).
- [44] Given the local steepness of ΔH , many points need to be computed close to that region in order to obtain substantial resolution grid in H^* .